

# Computer vision for automated experiments with superconducting qubits

G.Fedorov<sup>1, 2, a)</sup> and A. Ustinov<sup>1, 3</sup>

<sup>1)</sup>*Russian Quantum Center, Skolkovo village, Russia*

<sup>2)</sup>*Moscow Institute of Physics and Technology, Dolgoprudny, Russia*

<sup>3)</sup>*Karlsruhe Institute of Technology, Karlsruhe, Germany*

(Dated: 15 November 2018)

To build a full-scale quantum processor it is necessary to automate as many steps as possible on the physical, hardware level. Circuit quantum electrodynamics (cQED) is a contemporary architecture for dispersive readout and Purcell protection of superconducting qubits of various types, and thus it is necessary to develop software that is able to perform every kind of automatic calibration of such systems from scratch without any human participation. The first step towards this goal is to build a noise-insensitive and accurate computer vision tool to process the three-dimensional spectroscopic data that are ubiquitous in the domain. In this work we present and describe two widely-applicable and scalable algorithms that are capable to robustly and efficiently extract all Hamiltonian parameters from the spectroscopic data.

## I. MOTIVATION

Experiment automation, automatic data processing and decision making is vital in developing even a small scale quantum processor. For superconducting qubits, large companies such as Google<sup>1</sup>, Rigetti<sup>2</sup> and IBM<sup>3</sup> already use to some extent automated procedures for calibration of the qubit parameters and tuning up the single and two-qubit gates. This is not surprising since performing experiments with superconducting qubits is usually quite demanding in terms of human time. For example, to fully characterize a tunable transmon qubit coupled to a resonator (which assumes extracting the Hamiltonian parameters and coherence times) in an ideal scenario one would need to perform at least 10 individual measurements of different kinds<sup>4,5</sup>. Each of those experiments needs constant monitoring and parameter adjustments which may take days if, for example, several qubit chips are being examined. Moreover, more elaborate experiments such as measuring the coherence times versus some control parameters combinations or versus time are just impossible to do by hand despite having tremendous value to the characterization of the fabrication technology<sup>6,7</sup>.

Nonetheless, the subject is not represented abundantly in academic literature, and some experiments, for example, spectroscopy, are still being executed by hand<sup>5</sup>. Possibly, this can be attributed to the fact that it is not straightforward to implement a fully autonomous system that would be able to handle the experiment from the very beginning. While in research this state of affairs is acceptable since even a human experimenter does not know beforehand what kind of algorithm he should apply, it is definitely a problem for the development of the quantum computing chips. To develop such system, firstly, it is necessary to create an efficient and robust processing tool that will be able to handle all kinds of experimental data and replace human operator in terms of extracting the

physical qubit parameters.

In this work, we are proposing and implementing several methods of data processing and computer vision that tremendously facilitate the spectroscopy of circuit QED<sup>8</sup> architectures widely used for the readout the qubit states. Our method is accurate, fast and robust to noise, is applicable to any type of superconducting qubit that has a periodic and parametrizable spectrum, and is fully compatible with the state-of-the-art paradigm of one readout resonator per one qubit<sup>9,10</sup>. This means that our approach is scalable and can be applied to processors with any number of qubits. To achieve this we have employed several optimization algorithms to find spectral data from the heatmap plots that are ubiquitous in the domain.

## II. BACKGROUND

The methods that we use are relying heavily on the theoretical formalism that describes the behaviour of the superconducting qubits and cQED systems<sup>11</sup>. Thus, below we are introducing briefly the key concepts and equations that will be used in the following sections.

Without significant loss of generality, we will consider a tunable transmon<sup>12</sup> qubit capacitively coupled to a notch-type readout resonator. This architecture is currently widely used<sup>6</sup> and therefore serves a good example to demonstrate the algorithms performance.

### A. Transmon qubit

The simplest version of this qubit consists of a Josephson junction shunted with a large capacitor. Flux tunability of the frequency is attained by replacing a single Josephson junction with a SQUID as in Fig. 1(a) and applying external magnetic flux  $\Phi_e$  to its loop. This configuration can be equivalently represented with a shunted junction of tunable energy, Fig. 1(b).

<sup>a)</sup>Electronic mail: gleb.fedorov@phystech.edu

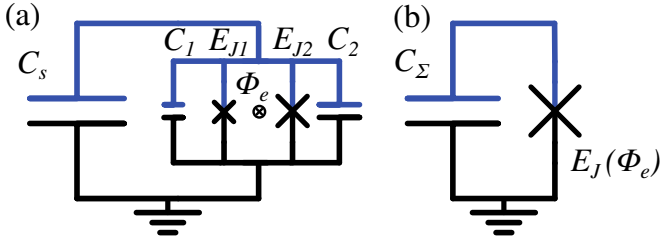


FIG. 1. (a) A tunable transmon circuit with an asymmetric SQUID,  $E_{J1} \neq E_{J2}$ . (b) Equivalent transmon with tunable energy  $E_J(\Phi_e)$  and unified capacitance  $C_\Sigma$ . The qubit island containing its single degree of freedom is in blue.

Level	Energy	Transition	Frequency
$g$ ( $E_0$ )	0	$ge$	$\omega_{ge}$
$e$ ( $E_1$ )	$\sqrt{8E_J E_C} - E_C$	$gf/2$	$\omega_{ge} - 0.5E_C$
$f$ ( $E_2$ )	$2\sqrt{8E_J E_C} - 3E_C$	$ef, gd/3$	$\omega_{ge} - E_C$
$d$ ( $E_3$ )	$3\sqrt{8E_J E_C} - 6E_C$	$ed/2$	$\omega_{ge} - 1.5E_C$
$E_4$	$4\sqrt{8E_J E_C} - 10E_C$	$fd, eE_4/3$	$\omega_{ge} - 2E_C$

TABLE I. Energies and some transition (single and multi-photon) frequencies for the first 5 levels of the transmon calculated with (3).

The Hamiltonian for such equivalent circuit is as follows:

$$\hat{H}_{tr} = 4E_C \hat{n}^2 - E_J(\Phi_e) \cos \hat{\phi}, \quad (1)$$

where  $E_{J1,2}$  are the Josephson energies,  $E_C = e^2/2C_\Sigma$ ,  $C_\Sigma = C_s + C_1 + C_2$ , is the charging energy,  $\hat{n}$  and  $\hat{\phi}$  are the operators for the Cooper pair number and the phase of the qubit island. For the equivalent Josephson energy  $E_J$  one obtains

$$E_J(\Phi_e) = E_{J\Sigma} \cos \phi_e \sqrt{1 + d^2 \tan^2 \phi_e}, \quad (2)$$

where  $E_{J\Sigma} = E_{J1} + E_{J2}$ ,  $\phi_e = \pi \Phi_e / \Phi_0$ ,  $d = \frac{E_{J1} - E_{J2}}{E_{J1} + E_{J2}}$  is the asymmetry of the SQUID. As one can notice, the dependence is periodic in  $\Phi_e$ . It is also possible to derive analytical expressions for the energy levels and transition frequencies for this type of qubits. The energy of the  $m^{\text{th}}$  level is<sup>12</sup>

$$E_m = m \sqrt{8E_J(\Phi_e) E_C} - \frac{E_C}{12} (6m^2 + 6m), \quad (3)$$

and some of the transition frequencies are presented in Table I. The qubit frequency  $f_{ge} = \omega_{ge}/2\pi$  may be approximated as

$$\sqrt{8E_J(\Phi_e) E_C} = f_{ge}^{\max} \sqrt{\cos \phi_e \sqrt{1 + d^2 \tan^2 \phi_e}},$$

$f_{ge}^{\max} = \sqrt{8E_J(0) E_C}$ , to make it depending on just two parameters instead of three.

## B. Circuit QED

The readout of the superconducting qubits is now predominantly done using an ancilla system which is usually implemented as a superconducting microwave resonator which

acts as an electromagnetic cavity in the standard cavity QED. Truncating the qubit to two levels, one may obtain the following Hamiltonian for the compound cavity-qubit system (in RWA):

$$\hat{H}/\hbar = \frac{\omega_q}{2} \hat{\sigma}_z + \omega_c \hat{a}^\dagger \hat{a} + g(\hat{\sigma}^- \hat{a}^\dagger + \hat{\sigma}^+ \hat{a}), \quad (4)$$

where  $\omega_q$  is the qubit frequency,  $\omega_c$  is the cavity frequency and  $g$  is the coupling strength. As long as the RWA is done, this Hamiltonian may be diagonalized analytically:

$$E_{g,0} = \frac{\omega_c - \omega_q}{2}, \quad (5)$$

$$E_{\pm,n} = (n+1)\omega_c \pm \frac{1}{2} \sqrt{4g^2(n+1) + (\omega_q - \omega_c)^2}. \quad (6)$$

This is very convenient for our purposes. By substituting the dependence of the qubit frequency  $\omega_q \equiv \omega_{ge} = 2\pi f_{ge}$  on some control parameter into these equations we can get straightforwardly the full system spectrum in dependence on that parameter. In Fig. 2 we have used the equations (3), (5) and (6) to model a tunable transmon interacting with a cavity for various  $\Phi_e$  and various  $f_{ge}^{\max}$ ,  $d$ . In the lower row of the figure, one can see that it is possible to extract the dependence of the cavity frequency  $\omega_c = 2\pi f_c$  on  $\Phi_e$ ; for example, the well-known avoided crossing pattern can be directly observed in Fig. 2(a), and the other two possible behaviours for the qubit entirely above or below the resonator in Fig. 2(b),(c). To shorten the notation, in the following we will define the corresponding branch frequencies of (6) as  $f_{\pm} = (E_{\pm,0} - E_{g,0})/2\pi$ .

In Fig. 2(a) it is also possible to see the entire spectrum of a transmon  $ge$  transition predicted by equations (2), (3). It has a cosine-like periodic shape with a period of one flux quantum  $\Phi_0$ . Consequently, it has two extrema, the upper and the lower which are called “sweet spots” due to the first-order insensitivity to  $\Phi_e$ , and thus to possible flux noise. In the following, by saying sweet spot we will assume the upper one whose frequency is  $f_{ge}(\Phi_e = 0) \equiv f_{ge}^{\max}$ .

We will use the model (5), (6) to fit the resonator frequency that we can find in an experiment. The only conceptual problem for the fitting that is left now is that the function we want to use as a model is not single-valued. Indeed, in Fig. 2(a, top) for each value of magnetic flux we always find two frequency points corresponding to the qubit and to the resonator, respectively. However, in practice only a narrow scan around the resonator frequency such as in Fig. 2(a, bottom) is required, and thus no ambiguity occurs.

## III. METHODS

In this section the actual algorithms that perform fitting and data extraction are discussed. Additionally, we describe important peculiarities of the data itself and some essential experimental details.

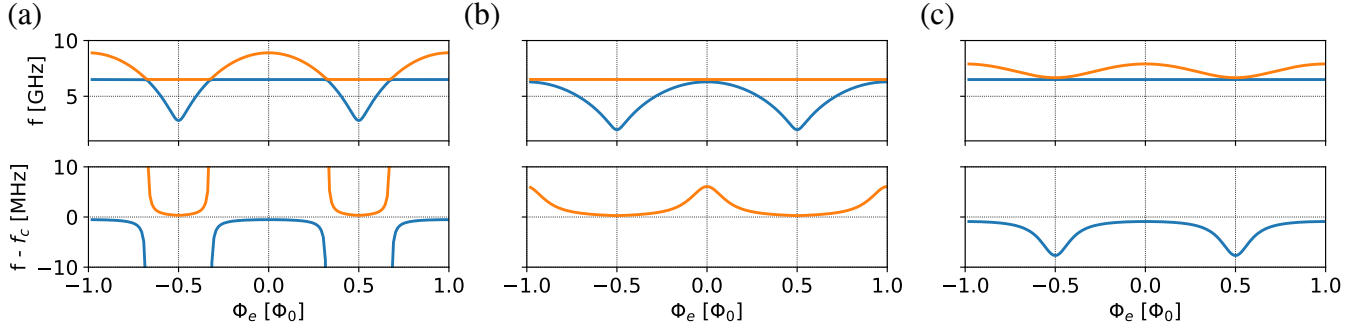


FIG. 2. Frequency spectrum of the transmon-resonator system. Parameters used:  $f_{ge}(0) \approx \sqrt{8E_C E_J(0)}/2\pi = 8.5$  GHz,  $d = 0.3$ ,  $f_r = 6.4$  GHz,  $g = 30$  MHz. For each subplot two transition branches  $f_{\pm} = (E_{\pm,0} - E_{g,0})/2\pi$  (orange and blue, respectively) both forming the resonator and qubit lines. As one can notice, there are three qualitatively different cases of the resonator-qubit disposition. Lower row shows a zoomed area around  $f_c$  that looks differently in each case.

### A. Analysing resonator spectra

In the real life applications, the spectrum of the resonator is usually recorded with a vector network analyzer which measures the complex scattering parameter  $S_{21}$  for each probe frequency  $f_p$  in a certain area around the resonance. Hence, after the VNA scan there are two 2D plots for the amplitude and the phase of the transmission versus frequency. When the magnetic flux sweep is added, the data becomes three-dimensional and has to be represented visually using a heatmap plot. One such heatmap for a notch-port resonator coupled to a transmon qubit is presented in Fig. 3(a). Please notice, that in all cases it is not possible to know which flux  $\Phi_e$  is applied to the SQUID. The experimenter usually knows only the current (or voltage) which he applies to some coil and which is connected linearly to  $\Phi_e$ :  $\Phi_e = MI + \Phi_r$ , where  $M$  stands for the mutual inductance of the coil and the SQUID, and  $\Phi_r$  is some residual flux. We will call the currents for the high and low transmon sweet spots  $I^{max}$ ,  $I^{min}$ , respectively.

The idea is to fit the image shown Fig. 3(a) with the model equations (5), (6). This task is not trivial because it belongs to a class of optimization problems where the loss function (i.e. in the least squares algorithm) is ill-defined. This is due to the periodic dependence of the frequencies on  $\Phi_e$  (and  $I$ ) and unknown position of the qubit sweet spot due to the local residual flux. Fortunately, it is possible to get a good initial guess for these parameters and then brute force the solution since we have a well defined bounds for each of the variables left.

The outline of the method which uses Fig. 3(a) as an example is presented below. The chosen type of the resonator-qubit arrangement which yields the avoided crossing pattern is not universal: there are two other cases when the qubit spectrum lies entirely below or above the resonator frequency, as in Fig. 2(b),(c). However, they are treated exactly the same way.

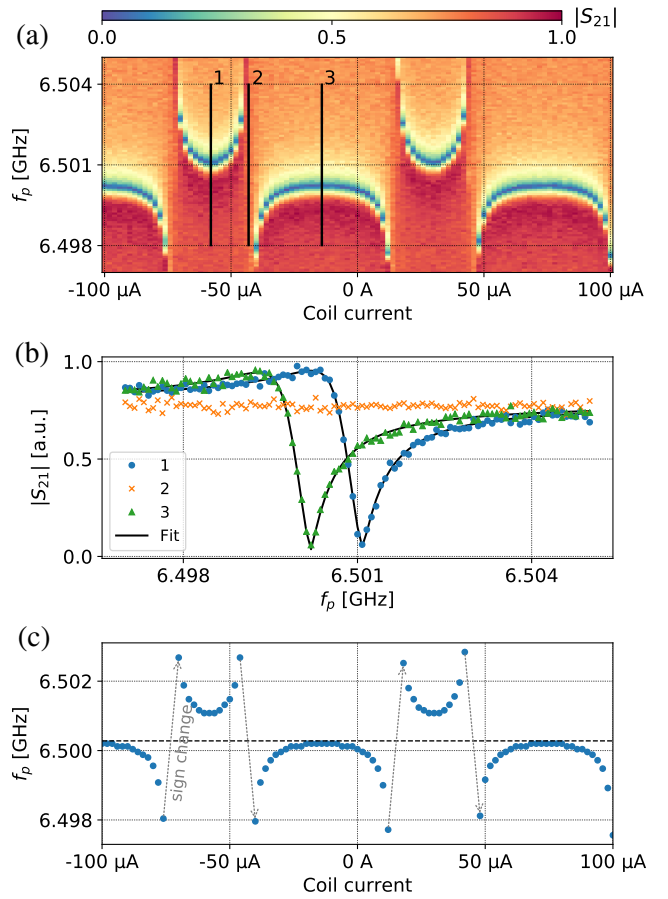


FIG. 3. (a) An experimental spectrum of a resonator strongly coupled to a transmon qubit depending on the coil current generating the magnetic flux  $\Phi_e$ . (b) Slices of the transmission from (a) showing two slices with fits (1,3) and a plateau with no dip (2) present. (c) Extracted data (blue dots) and mean frequency value over all points  $\langle f_r \rangle_{\Phi_e}$  (black dashed line). Grey arrows show where  $f_r - \langle f_r \rangle_{\Phi_e}$  changes sign.

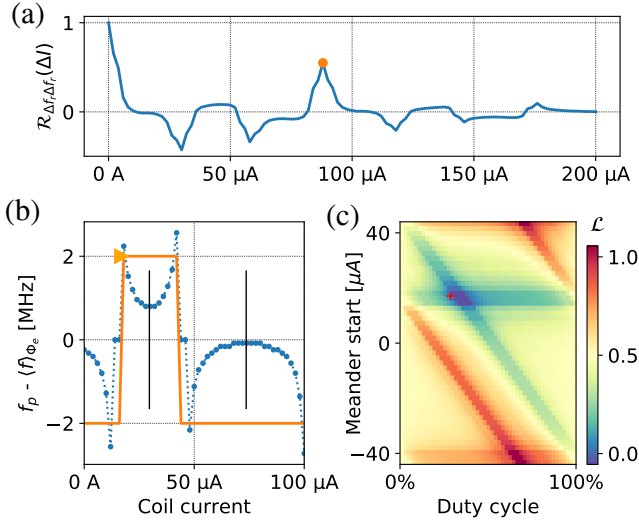


FIG. 4. Period and phase extraction procedure. (a) Autocorrelation function depending on the lag  $\Delta I$  shows a prominent local maximum at 88  $\mu\text{A}$  (orange dot). (b) Construction for phase estimation;  $\Delta f_r = f_r - \langle f_r \rangle_{\Phi_e}$  (blue) is fitted with a square wave (orange, start marked with a triangle). Vertical bars mark candidate sweet spots. (c) Loss function (normalized) for the square wave fitting procedure from (b); red cross indicates the parameters of the meander shown there.

### 1. Extracting $f_r(\Phi_e)$ from data

The first thing to do is to reduce the dimensionality of the data, i.e. extract the resonance frequency for each  $\Phi_e$  and then be left with the desired  $f_r(\Phi_e)$ .

We do this by employing the *circleft*<sup>13</sup> library which is capable of fitting various types of microwave resonators. For each  $\Phi_e$  we fit the complex transmission  $S_{21}(f)$  as in Fig. 3(b) (solid black lines) and extract the resonance frequency from the model. The only possible caveat is that for some  $\Phi_e$  values the resonance dip may disappear (see Fig. 3(b)) and the fit will fail. Such slices are thus excluded in advance via a threshold condition.

The resulting plot of extracted frequency is shown in Fig. 3(c) with blue dots. There are some current values located between the branches for which the points are missing, as expected. Additionally, we plot here another key parameter which is the mean value of the detected frequencies shown as a dashed black line. Firstly, this parameter will serve as an initial guess for the cavity frequency of the model (5), (6):  $f_c \approx \langle f_r \rangle_{\Phi_e}$ . Secondly, it serves as a baseline used in the following period and phase extraction algorithm which tracks the changes of the sign of the value  $\Delta f_r = f_r - \langle f_r \rangle_{\Phi_e}$  (marked as grey dashed lines in Fig. 3(c)). These sign changes are crucial in determining the location of the qubit sweet spot.

### 2. Extracting period, phase and sweet spot locations

As we have said above, one of the serious obstacles for the fitting is that the periodicity of the data on one of the fitting

parameters. Along with the equally unknown phase of the signal, this leads to the presence of many local minima in the loss function which severely impeded the progress of iterative optimization algorithms. In other words, the unknown coefficients  $M$  and  $\Phi_r$  in the dependence of  $\Phi_e$  on the coil current  $I$  are preventing us to find the global minimum we need. Fortunately, it is possible to find the period and the phase (or, alternatively,  $\Phi_r$ , or the sweet spot location) of the data without fitting the full model Eqs. (5), (6) which alleviates the stated problem. Of course, in the absence of noise, this would be a trivial task. However, in the real-life conditions the noise to some extent is always present, so below we engineer a solution that is insensitive to local sporadic perturbations of the data.

A very powerful tool for finding the period  $\Pi_f$  in a given dataset  $y$  especially when it contains just a few periods is the autocorrelation function  $\mathcal{R}_{yy}(l) = \sum_n y_n y_{n-l}$ . The location of the largest of its local maxima (except for the  $l = 0$ ) equals exactly the sought period. However, this is only true when the mean value of the function is zero; otherwise,  $\mathcal{R}_{yy}(l)$  would be linear with a very steep slope smearing out all the extrema. Therefore, instead of  $f_r(\Phi_e)$  we consider the function  $\Delta f_r(\Phi_e)$  introduced above which has zero mean and the same period. For this function, which looks exactly like one from Fig. 3(c) but centered vertically around zero, the autocorrelation function  $\mathcal{R}_{\Delta f_r \Delta f_r}(\Delta I)$  is shown in Fig. 4(a). As one can see, it depends on the current offset  $\Delta I$  which spans 200  $\mu\text{A}$  just as the data itself. This means that the data is being zero-padded at all  $\Delta I$  except for  $\Delta I = 0$ , and this is why we get a diminishing value of the correlation peaks when the lag reaches  $\Pi_f$  or  $2\Pi_f$ . The orange dot in the plot shows the highest local extremum of  $\mathcal{R}_{\Delta f_r \Delta f_r}(\Delta I)$  at 88  $\mu\text{A}$ . It is a very prominent peak and can be easily distinguished among all others. There is as well a small peak at 176  $\mu\text{A}$  which corresponds to  $\Delta I = 2\Pi_f$ . Note that the autocorrelation function is not smooth. This is because there were some missing points in the data (corresponding to the plateaus of Fig. 3(b)) that were replaced by zeros to ensure correct mapping between current indices and current values. This can be noticed as well in Fig. 4(b).

Now, having found the period it is possible to precisely determine the phase of the signal. This is done via finding a global maximum of zero-lag correlation function  $\mathcal{R}_{\Delta f_r S}(0)$  of  $\Delta f_r$  with a square wave  $S(I, \Pi_f, \phi, D)$  signal having the same period but unknown phase  $\phi$  and duty cycle  $D$ . An illustration of a meander function satisfying the optimal condition is presented in Fig. 4(b) in orange. The phase  $\phi$  (in  $\mu\text{A}$ ) denotes the x-coordinate of the first point after the rising edge, and is marked with a triangle. The high and low levels of the square must be opposite in value, i.e. 1 and -1, and the absolute value does not matter. Generally, the idea behind this is to robustly detect sign changes that were shown back in Fig. 3(c). We can not rely on a more simple algorithm that walks through the points and marks where the function changes its sign because such algorithm will fail in the presence of a strong noise. Conversely, the optimization algorithm described above is not sensitive to local short-term sign changes.

The global optimal  $\phi$  and  $D$  are found using a brute force algorithm. It calculates the loss function  $\mathcal{L} = -\mathcal{R}_{\Delta f_r S}(0)$  on a

$50 \times 50$  grid of  $(\phi, D)$  and takes the minimal value of all. It is feasible due to the evident boundaries on  $\phi \in [-\Pi_{f_r}/2, \Pi_{f_r}/2]$  and  $D \in [0, 1]$ . The loss function topography for the avoided crossing patterns is nicely structured and for our example is shown in Fig. 4(c). One can see that instead of a single minimum it has an area of the same minimal value. Again, the roots of this effect lie in the missing  $f_r$  points. However, any value from this valley suits well enough for our purposes, and the algorithm finds no difficulty in locating it.

With values for  $\Pi_{f_r} = \Phi_0/M$ ,  $\phi$  and  $D$  we now can calculate the currents of the two transmon sweet spots in the case of the avoided crossings pattern:

$$I^{max} = \phi + \Pi_{f_r} \left( \frac{1+D}{2} \right) = \Phi_r/M, \quad (7)$$

$$I^{min} = \phi + \Pi_{f_r} \left( \frac{D}{2} \right). \quad (8)$$

For the smooth dependences Fig. 2(b)-(c) the situation is opposite:  $I^{max(min)} \rightarrow I^{min(max)}$ . To distinguish the two cases when the noise is not large, it is enough to calculate the maximal differential of the frequency data and compare it to its peak-to-peak amplitude. For the avoided crossings these values are close and for the smooth curves they are not. However, in the presence of noise this indicator will fail, and we will have to resort to checking both current values for being  $I_{max}$  based on the best fit among the two possibilities.

### 3. Full model fitting and testing

Having performed the aforementioned preliminary steps, it is now possible to fit the full model to the extracted points. To do this, we employ brute force optimization combined with Nelder-Mead<sup>14</sup> search. Firstly, we define the loss function for the problem as follows. For the known probe frequency span of the data  $\Delta f_p$  (Fig. 3(a), whole y-axis) and the set of  $N$  extracted points  $\{p_i\} = \{(I_i, f_{r,i})\}$ , we define the loss function per one point as

$$\mathcal{L} = \frac{1}{N} \sum_{i=0}^N [f_i - \mathcal{M}(MI_i + \Phi_r, f_c, g, f_{ge}^{max}, d)]^2, \quad (9)$$

$$\mathcal{M} = \begin{cases} f_+, & |f_+ - f_c| < \Delta f_p/2 \\ f_-, & \text{otherwise,} \end{cases} \quad (10)$$

where, as in the previous section,

$$f_{\pm} = f_{\pm}(MI_i + \Phi_r, f_c, g, f_{ge}^{max}, d) = E_{\pm,0} - E_{g,0}.$$

The condition of Eq. (10) means that we choose only the frequencies that lie within a window  $\Delta f_p$  around the model  $f_r$  parameter. This ensures, firstly, that in the optimum we will not take any excess points outside the frequency scan, and, secondly, that we have a single model value for each current.

To substantiate the choice of the optimization algorithms, we present in Fig. 5 three visualizations of the the defined loss function. The plots show how the function behaves if a certain pair of 6 model parameters is varied. From the plots

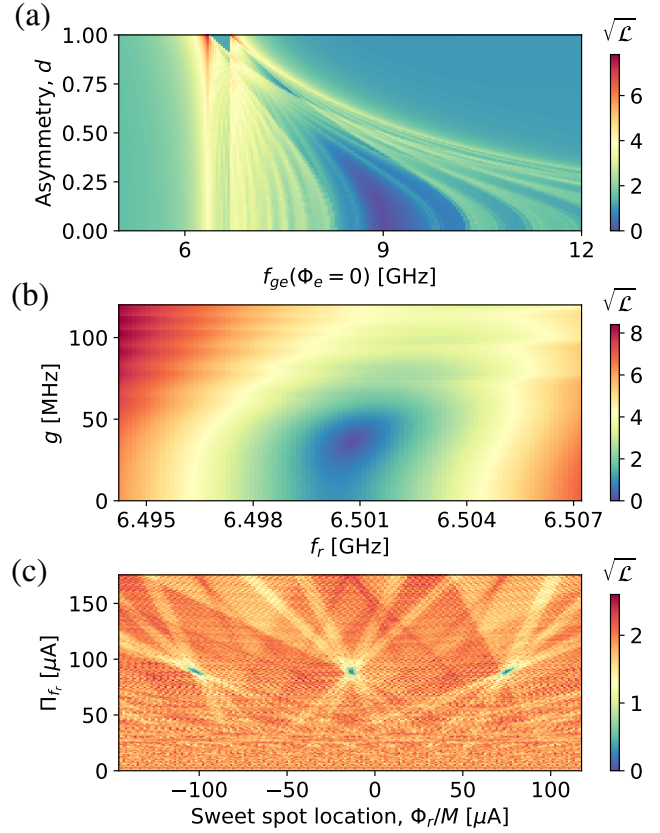


FIG. 5. Slices of the loss function (9) for the full model and experimental data from the example made around the optimal point. Root-mean-square per-point loss  $\sqrt{\mathcal{L}}$  is in MHz. (a)  $f_{ge}^{max}$  and  $d$  are varied, other parameters optimal. A large valley is located near 9 GHz, and some smaller locally minimal ones are present all around. (b)  $g$  and  $f_r$  are varied, others optimal. The loss function for these two parameters is well-conditioned near the optimum. (c) Period  $\Pi_{f_r} = \Phi_0/M$  and  $\Phi_r/M$  varied, others optimal. This subplot illustrates a complex structure of local minima around the true one which we find analytically.

it is obvious that it is ill-defined and has a lot of local minima which would impede robustness in real life applications. The  $f_{ge}^{max}$  and  $d$  parameters present the most significant difficulty in terms of false minima as can be seen from Fig. 5(a). In contrast,  $f_r$  presents the least difficulty, as can be seen from Fig. 5(b). The last plot Fig. 5(c) shows a very complex structure of the loss function and a very small-sized optimal valley and serves as an illustration of why the period and phase extraction is important.

The brute force algorithm acts on the grid specified in Table II. The ranges in the grid are based on the usual design parameters of the modern qubit samples and the number of steps is chosen to be able to catch the optimal valley in the loss function.

After the coarse brute force optimization is done and the optimal valley is located, we apply the Nelder-Mead simplex downhill algorithm to polish the brute force result. This algorithm works very well in our case, as one can see from the



Parameter	Value range	Steps #	Brute est.	Final
$M$	$\Phi_0/\Pi_{f_r}$	1	11.4 $\Phi_0/\text{mA}$	same
$\Phi_r$	$M I^{max}$	1	-0.13 $\Phi_0$	same
$f_c$	$\langle f_r \rangle_{\Phi_e} \pm 1 \text{ MHz}$	3	6.5003 GHz	6.5007 GHz
$g$	20 - 40 MHz	5	24 MHz	36.1 MHz
$f_q^{max}$	4 - 12 GHz	80	8 GHz	8.9 GHz
$d$	0 - 0.9	9	0.5	0.08

TABLE II. Grid specifications for the brute force algorithm and the resulting optimal points. The number of steps is taken with some margin to ensure correct location of the optimal valley even for difficult cases. The optimal parameters estimated by brute force and the final ones have the RMS loss values of 0.258 MHz and 0.024 MHz, respectively.

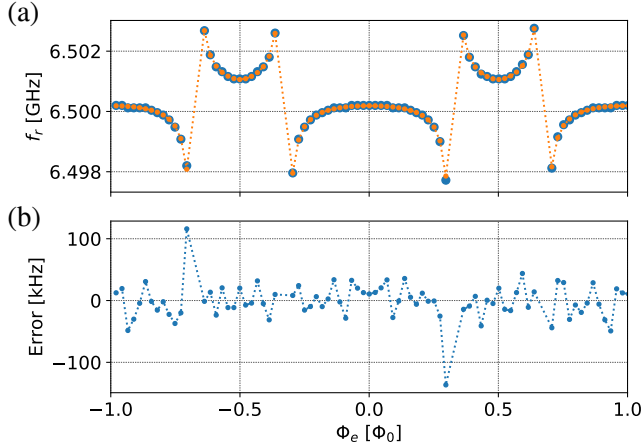


FIG. 6. The result of the algorithm execution. (a) The data (blue dots) and the model (orange connected dots). (b) Residual error which is mostly random and is of order of 25 kHz per point.

Table II comparing the brute estimation and the final result after Nelder-Mead is performed. The significant improvement in the loss value of the polished result compared to the brute estimation is due to the more accurate determination of the cavity frequency  $f_c$  which leads as well to major shifts in optimal  $g$ ,  $f_q^{max}$  and  $d$ .

Finally, the resulting fit is presented in Fig. 6 along with the plot of the residuals. The match is almost perfect, and the noise in the residuals is random and thus shows no systematic errors. In Fig. 7 we also present the fitting results for different powers of added noise. The signal-to-noise ratio (SNR) is defined for our data in a similar manner as the SNR in the resonator fitting tests<sup>13</sup>; we take distance  $2r$  between two maximally remote points of  $S_{21}(f_p, \Phi_e)$  among any pair on the complex plane (i.e., the diameter of the resonance circle) as the signal amplitude, and the noise of the form  $\frac{\xi_1 + i\xi_2}{\sqrt{2}}$ , where  $\xi_1, \xi_2$  distributed normally with zero mean and variance (amplitude)  $\sigma$ . The SNR then is defined as  $r/\sigma$ . As one can see from the graph, the algorithm stays robust even at very low SNRs that are even lower than the low limit SNRs for the *circlefit* stability. This is possible because a fallback strategy of taking the smallest amplitude point as the resonance is applied

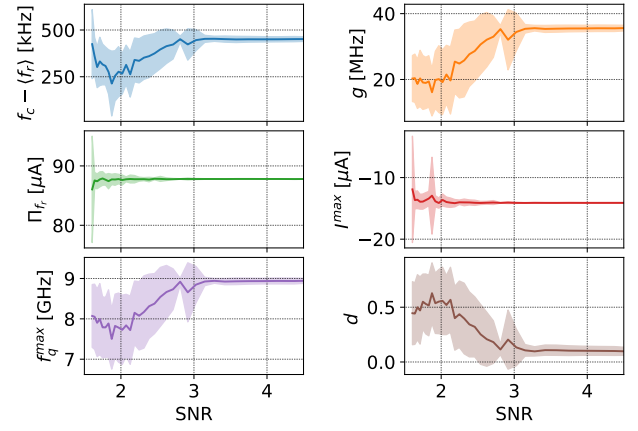


FIG. 7. Behaviour of the algorithm on the data with the gaussian noise of varying noise power added. The clouds show standard deviations of optimal parameters after 50 tries, solid lines show mean values. The algorithm is very stable above SNR=8 but is still robust at detecting avoided crossings down to SNR=3-4 but with reduced accuracy in  $f_q^{max}$ ,  $g$  and  $d$ . Other three parameters are still very accurate.

when *circlefit* fails. Ultimately, the key point of this stress test is to show that the algorithm can be applied in real-life scenarios when the data may be of low quality.

The fitting algorithm was implemented in Python using brute and Nelder-Mead routines from Scipy. The fitting example above runs for 3.2 seconds on a 5-year old Intel Core i5-3337U CPU, from which 2.7 seconds are for the brute and 0.4 of a second is for the Nelder-Mead minimization. On a contemporary Intel Core i7-7700 CPU, it takes about one second to run the whole procedure. The time costs mostly come from the square root calculation necessary for Eqs. (3) and (6) and because that the brute routine is not parallelized. However, this is still fast, firstly, because recording a resonator spectrum such as one in the example takes around 20 seconds, and, secondly, it is much faster than a human would do.

We have tested the algorithm on more than 100 real spectra that we have in our experimental database, and it finds an optimum for any kind of the dependence of the resonance on the flux caused by various dispositions of the qubit and the resonator, as in Fig. 2(b),(c). Example fitting results for these cases are provided in Fig. 8. There is a caveat, however, in some of such cases. It turns out, that for large qubit-cavity detunings two different sets of parameters that are minimizing the loss function equally well are possible. An illustration for this statement can be seen in Fig. 9(a),(b). The algorithm was launched using different grid ranges for  $f_q^{max}$ . In one case (orange) the search was done below, and in the other (green) above the mean resonance frequency  $\langle f_c \rangle_{\Phi_e}$ . The resulting fits are equally accurate, and without other information about the system it would not be possible to choose between these two cases. Therefore, some hints may be passed to the algorithm, for instance, whether to look for the qubit above or below the resonator. Otherwise, it would be necessary to check both possibilities with other methods, i.e. via two-tone spectroscopy.

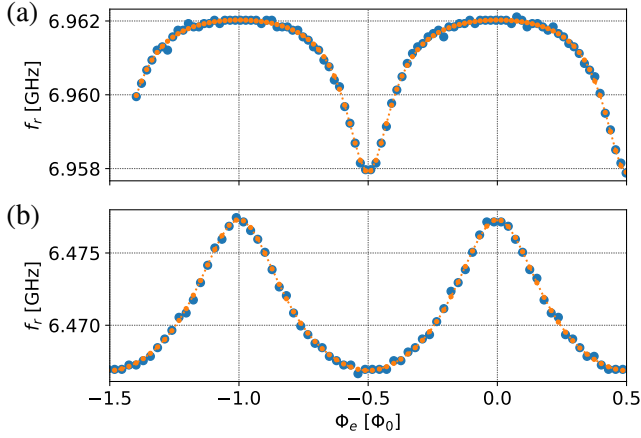


FIG. 8. Fitting two other samples of our dataset presenting other two possible cases (blue dots are data, orange connected dots are the model). (a) The qubit is entirely above the resonator. Per-point RMS error is 60 kHz. (b) The qubit is below the resonator. Error is 150 kHz (larger due to the proportionally larger amplitude of the frequency variation).

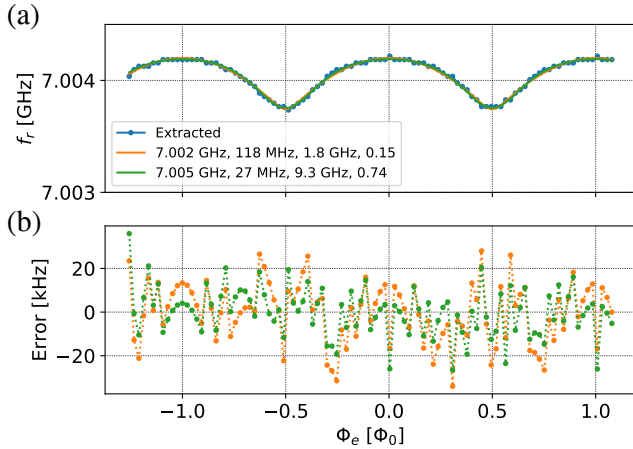


FIG. 9. (a) Two alternative fits (orange and green lines) for the same data (blue dots). The corresponding parameters  $f_c$ ,  $g$ ,  $f_q^{max}$ ,  $d$  for the two alternative fits are shown in the legend. (b) Residuals for the two fits, in orange (qubit below) and green (qubit above). RMS errors are 14 kHz and 11 kHz, respectively.

## B. Analysing qubit spectra

Unfortunately, the resonator fitting procedure accuracy in terms of the qubit frequency ( $>100$  MHz) is not enough in practical applications where it is necessary to obtain exact value of the qubit frequency down to 1-10 MHz. For the cQED systems, it may be done, in general, by trying to excite the qubit at different frequencies and then read it out expecting the  $e$ -state to be measured. The task is to find the exact location and shape of all the spectral lines depending on the magnetic flux that will be detected using such a method.

Particularly, in many groups, the qubit spectrum is searched for using the so-called two-tone spectroscopy<sup>15</sup>. It consists

of sending two microwave signals at the cQED system from which one, the probe tone, has a fixed frequency near  $f_c$ , and the frequency  $f_{exc}$  of the other, excitation tone, is varied. When the second signal becomes resonant with some transition (i.e., qubit  $ge$  transition), a shift of the cavity frequency occurs, and thus the transmission at the frequency of the first tone changes. This way, a heatmap showing the dependence of the frequency of various system transitions on the magnetic flux can be obtained.

An example from our database for a tunable transmon coupled to a notch-port resonator is displayed in Fig. 10. To obtain the two-tone spectrum in Fig. 10(b), for each current value the frequency of the first tone  $f_p$  is chosen to be equal to the frequency of the minimal transmission from the single-tone spectroscopy (STS), see Fig. 10(a). At the avoided crossing, this is not possible, and thus the frequency  $f_p$  may be chosen to be arbitrary within the scan area of the STS. This does not pose a problem since the two-tone spectroscopy is still only effective when the qubit and the resonator are detuned far from each other, i.e. in the dispersive regime<sup>11</sup>, and would not work well near the resonant regime.

The resulting plot Fig. 10(b) shows the dependence of  $S_{21}$  on the magnetic flux and the excitation frequency. Most of the scan is in blue meaning that the resonator is not shifted and the probe tone gets almost entirely reflected (see colorbar). However, there are some different colour areas. Firstly, a bright and narrow horizontal line is observed near 6.5 GHz where the resonator is located. Likewise, there are two sharp horizontal lines just above 6.75 GHz which are from the crosstalk coupling to another on-chip resonator. Secondly, bright vertical stripes are seen at the current values corresponding to the

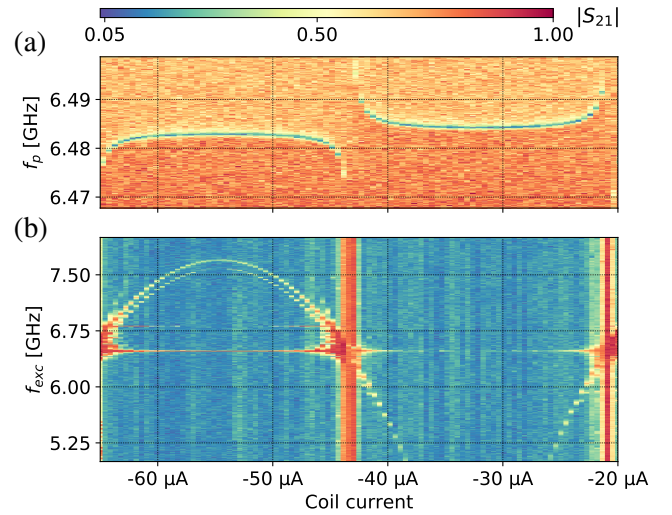


FIG. 10. Two types of spectroscopy results side by side; the colorbar is common, coil current scan range is the same. (a) Single-tone spectroscopy (one period on  $\Phi_e$ ). (b) Two-tone spectroscopy result. Clear flux-dependent transmon transitions are visible ( $ge$  and  $gf/2$ ), and some fixed-frequency resonator excitations are present as well. Red vertical stripes are observed when the qubit and the cavity are close to resonance.

avoided crossing areas. Finally, two transmon transitions of varying frequency are visible. The upper one is the  $ge$  transition, and the lower one is the two-photon  $gf/2$  one; at each coil current, they are separated by  $E_C/2h$ , or half the anharmonicity of the transmon (see Table I).

The presence of several bright lines along with noise makes it in general impossible to accurately fit the data with the model (3) using the standard curve fitting procedures. Additionally, when several multi-photon transitions are visible, it is hard for an algorithm to distinguish between them to find only the  $ge$  transition. This means that for robust qubit detection we need to fit all possible single- and multi-photon spectral lines simultaneously. Below, we present our approach to solve this problem.

### 1. Extracting data points

Similar to the reasoning in section III A 1, the first thing to do is to reduce the three-dimensional picture Fig. 10 to two dimensions. This is done in several steps.

First, we calculate the mean transmission  $\langle S_{21} \rangle_{f_{exc}}(\Phi_e)$  for each current value. This operation gives us the background dependent only on  $\Phi_e$  and not on  $f_{exc}$ . This background can be then subtracted from the data, and the absolute value of the difference  $Z = |S_{21} - \langle S_{21} \rangle_{f_{exc}}|$  may be then plotted. For the example, the resulting image can be seen in Fig. 11. As one can notice, the background subtraction removes most of the vertical stripes that could be seen in Fig. 10(b).

Next, the data points may be extracted to form a 2D point array where the qubit lines may be searched for. This procedure is done in several steps. First of all, it is necessary to do thresholding of the data to obtain a binary image. We have tested various thresholding methods, i.e. Otsu's method<sup>16</sup>; however, the best performance in distinguishing local peaks from background was obtained using another method that is based on estimating the noise in the data. We estimate noise level  $\sigma$  by calculating the numerical difference between adjacent points in a row for each flux value, and then calculate the median absolute value:

$$\sigma = \text{median}_{i,j} (|Z_{i,j+1} - Z_{i,j}|),$$

where  $i$  numerates magnetic flux values, and  $j$  numerates excitation frequency values. Using median instead mean reduces the impact of singular bright extrema that may be present in the row.

Next, for each row we use the *find\_peaks* routine of the Scipy library to detect all local extrema there, and then exclude those whose height is less than  $\sigma$  as probably originating from the noise.

After finishing the procedures above, we get an array of points that correspond to the most prominent peaks in the data. However, already at this point it is possible to remove all points that come from the fixed-frequency resonator spectral lines. This is done by excluding horizontal rows of points that have exactly the same frequency value within the resolution of the data.

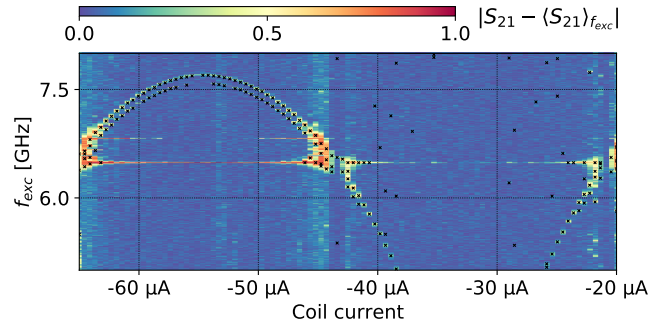


FIG. 11. Processed data and extracted and filtered datapoints (black crosses) that will be subject to fitting.

The final extracted points are shown in Fig. 11 in black crosses. As one can see, the horizontal lines are correctly not included, and two qubit lines are almost fully represented. Background noise is mostly ignored, too.

### 2. Fitting binary data

In most cases, even the filtered binary data contains noise and, importantly, is not single-valued for each flux value. This means that standard curve fitting methods are not applicable, and thus we resort to a hybrid algorithm that combines features of Hough transform<sup>17</sup> and local optimization.

The key construction for the algorithm is the loss function. The main idea behind it is illustrated in Fig. 12. Three narrow frequency bands of  $\Delta f$  are chosen around the model spectral lines. Points outside the bands are considered far away and are ignored. All the points inside a band are attributed to its line and included in its loss function. If at a certain flux there are several points inside a band, only the closest one is chosen and the rest (contentious) are ignored.

The full loss function is then constructed as follows. Let  $P_{1,2,3}$  be the sets of points selected for corresponding transition lines  $ge, gf/2, gd/3$ ; let the number of points in the sets be  $N_{1,2,3}$ , and  $N$  is the whole number of selected points, and  $N_0$  is the number of points in magnetic flux; let  $D_{1,2,3}$  be the corresponding vertical distances between the selected points and the model. Then the loss function is:

$$\mathcal{L} = \begin{cases} \frac{1}{N^2} \sum_{i=1}^3 (\sum_{P_i} D_i / N_i), & N_1 > N_0/2 \\ \sum_{P_1} D_1 / N_1 & \end{cases} \quad (11)$$

This loss function has two parts in it. First one works at the coarse scale. As one can notice, if the data points mostly come from the spectral lines, the loss function has a deep min

<sup>1</sup>J. Kelly, P. O'Malley, M. Neeley, H. Neven, and J. M. Martinis, "Physical qubit calibration on a directed acyclic graph," arXiv preprint arXiv:1803.03226 (2018).

<sup>2</sup>B. J. Bloom, S. A. Caldwell, M. Reagor, and C. Rigetti, U.S. Patent No. US 20180260732A (13 Sep. 2018).

<sup>3</sup><https://quantumexperience.ng.bluemix.net>.



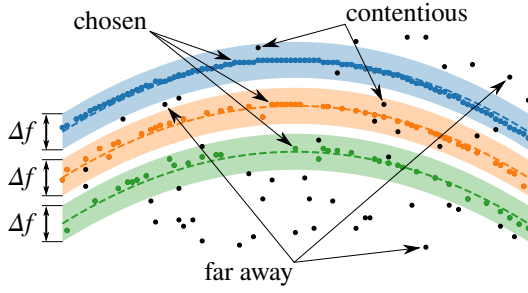


FIG. 12. An illustration for the loss function definition. In different colours are the frequency bands and selected points, black points are ignored.

<sup>4</sup>Resonator characterization, single-tone spectroscopy, two-tone spectroscopy, excitation and readout power calibration, IQ mixer calibration, Rabi oscillations, Ramsey oscillations, fine excitation frequency adjustment, fine  $\pi$ -pulse adjustment,  $T_1$ ,  $T_2$ ,  $T_{2E}$  measurements.

<sup>5</sup>S. M. Smith, *Metrology of Quantum Control and Measurement in Superconducting Qubits*, Ph.D. thesis, University of California Santa Barbara (2018).

<sup>6</sup>R. Barends, J. Kelly, A. Megrant, D. Sank, E. Jeffrey, Y. Chen, Y. Yin, B. Chiaro, J. Mutus, C. Neill, *et al.*, “Coherent josephson qubit suitable for scalable quantum integrated circuits,” *Physical review letters* **111**, 080502 (2013).

<sup>7</sup>P. Klimov, J. Kelly, Z. Chen, M. Neeley, A. Megrant, B. Burkett, R. Barends, K. Arya, B. Chiaro, Y. Chen, *et al.*, “Fluctuations of energy-relaxation times in superconducting qubits,” *Physical review letters* **121**,

090502 (2018).

<sup>8</sup>A. Blais, J. Gambetta, A. Wallraff, D. Schuster, S. Girvin, M. Devoret, and R. Schoelkopf, “Quantum-information processing with circuit quantum electrodynamics,” *Physical Review A* **75**, 032329 (2007).

<sup>9</sup>R. Versluis, S. Poletto, N. Khammassi, B. Tarasinski, N. Haider, D. Michalak, A. Bruno, K. Bertels, and L. DiCarlo, “Scalable quantum circuit and control for a superconducting surface code,” *Physical Review Applied* **8**, 034021 (2017).

<sup>10</sup>J. Kelly, R. Barends, A. G. Fowler, A. Megrant, E. Jeffrey, T. C. White, D. Sank, J. Y. Mutus, B. Campbell, Y. Chen, *et al.*, “State preservation by repetitive error detection in a superconducting quantum circuit,” *Nature* **519**, 66 (2015).

<sup>11</sup>A. Blais, R.-S. Huang, A. Wallraff, S. M. Girvin, and R. J. Schoelkopf, “Cavity quantum electrodynamics for superconducting electrical circuits: An architecture for quantum computation,” *Physical Review A* **69**, 062320 (2004).

<sup>12</sup>J. Koch, M. Y. Terri, J. Gambetta, A. A. Houck, D. Schuster, J. Majer, A. Blais, M. H. Devoret, S. M. Girvin, and R. J. Schoelkopf, “Charge-insensitive qubit design derived from the cooper pair box,” *Physical Review A* **76**, 042319 (2007).

<sup>13</sup>S. Probst, F. Song, P. Bushev, A. Ustinov, and M. Weides, “Efficient and robust analysis of complex scattering data under noise in microwave resonators,” *Review of Scientific Instruments* **86**, 024706 (2015).

<sup>14</sup>J. A. Nelder and R. Mead, “A simplex method for function minimization,” *The computer journal* **7**, 308–313 (1965).

<sup>15</sup>A. Wallraff, D. Schuster, A. Blais, J. Gambetta, J. Schreier, L. Frunzio, M. Devoret, S. Girvin, and R. Schoelkopf, “Sideband transitions and two-tone spectroscopy of a superconducting qubit strongly coupled to an on-chip cavity,” *Physical Review Letters* **99**, 050501 (2007).

<sup>16</sup>N. Otsu, “A threshold selection method from gray-level histograms,” *IEEE transactions on systems, man, and cybernetics* **9**, 62–66 (1979).

<sup>17</sup>P. V. Hough, “Method and means for recognizing complex patterns,” (1962), uS Patent 3,069,654.